

---

# Single Image Reflection Removal via inter-layer Complementarity

---

**Yue Huang**<sup>1</sup>

Guangdong University of Technology  
17324004911@163.com

**Zi'ang Li**<sup>1</sup>

Guangdong University of Technology

**Tianle Hu**<sup>1</sup>

Guangdong University of Technology

**Jie Wen**<sup>4</sup>

Harbin Institute of Technology

**Guanbin Li**<sup>2</sup>

Sun Yat-sen University

**Jinglin Zhang**<sup>3</sup>

Shandong University

**Guoxu Zhou**<sup>1</sup>

Guangdong University of Technology

**Xiaozhao Fang**<sup>1†</sup>

Guangdong University of Technology

## Abstract

Although dual-stream architectures have achieved remarkable success in single image reflection removal, they fail to fully exploit inter-layer complementarity in their physical modeling and network design, which limits the quality of image separation. To address this fundamental limitation, we propose two targeted improvements to enhance dual-stream architectures: First, we introduce a novel inter-layer complementarity model where low-frequency components extracted from the residual layer interact with the transmission layer through dual-stream architecture to enhance inter-layer complementarity. Meanwhile, high-frequency components from the residual layer provide inverse modulation to both streams, improving the detail quality of the transmission layer. Second, we propose an efficient inter-layer complementarity attention mechanism which first cross-reorganizes dual streams at the channel level to obtain reorganized streams with inter-layer complementary structures, then performs attention computation on the reorganized streams to achieve better inter-layer separation, and finally restores the original stream structure for output. Experimental results demonstrate that our method achieves state-of-the-art separation quality on multiple public datasets while significantly reducing both computational cost and model complexity.

## 1 Introduction

Reflection phenomena are ubiquitous and significantly degrade the quality of images captured through transparent media such as glass. This issue impacts various important domains, including autonomous driving and industrial specular surface inspection. Early research adopted idealized linear superposition models  $I = T + R$ [4], where  $I$  represents the observed image,  $T$  denotes the transmission layer, and  $R$  represents the reflection layer. However, these models failed to consider inter-layer complementarity. To address this limitation, researchers subsequently proposed weighted linear models such as  $I = \alpha T + \beta R$ [23], which began to recognize asymmetric complementary characteristics between the layers. While these models represented an improvement, they were still constrained by globally fixed weights. More recently, the general framework  $I = T + R + \Phi(T, R)$ [10] has marked a significant breakthrough by incorporating a learnable nonlinear residual function

$\Phi(T, R)$ . This approach can adaptively model complex inter-layer complementary relationships that linear methods cannot capture.

However, in-depth analysis of this framework and other mainstream methods reveals two critical problems: significant data heterogeneity and insufficient utilization of degradation cues. The data heterogeneity problem primarily stems from inconsistent supervision targets during training. Specifically, models are often supervised by reflection images  $R$  when processing synthetic datasets, but switch to using residual images (constructed as  $I - T$ ) as supervision for real datasets. This inconsistency significantly impacts the model’s generalization capability. On the other hand, insufficient utilization of degradation cues arises because using reflection images for supervision fails to capture degradation cues such as color shifts and contrast attenuation in the transmission layer. While using residual images appears to address both problems by providing consistent supervision targets and capturing dual degradation information from both reflection and transmission layers, this approach inevitably introduces unpredictable noise patterns due to the construction method of residual images, thereby compromising overall performance.

Based on these analyses and an understanding of inter-layer complementarity, we propose an innovative solution: uniformly using low-frequency residual image supervision on both real and synthetic datasets to construct a low-frequency residual flow that performs dual-stream interaction with the transmission flow. This approach fully leverages the robustness of low-frequency components in residual images, establishing a stable separation foundation while avoiding high-frequency noise. Building on this dual-stream architecture, we use dual-stream features to construct a high-frequency residual layer for reverse fine-tuning, which helps refine fine details in the transmission layer. This comprehensive approach addresses data heterogeneity and fully exploits degradation cues, significantly improving image demixing performance.

Moreover, leveraging the dual-stream interactive framework proposed by Hu and Guo [9], the DSIT method [11] introduces a novel Dual-Attention Interactive (DAI) mechanism. The core innovation of DAI lies in explicitly modeling intra-layer and inter-layer relationships of dual-stream features through attention mechanisms. Specifically, DAI concatenates dual-stream features along batch and window dimensions, then performs self-attention computation to capture feature correlations. However, although this approach can establish intra-layer and inter-layer associations in dual-stream space, it has not explored inter-layer complementarity in dual-stream channels. To address this limitation and explore such potential, we propose an inter-layer complementary attention mechanism based on channel-level cross-reorganization. Our key innovation differs from DAI in that we perform cross-reorganization of dual-stream features at the channel dimension. Instead of simple concatenation, we rearrange the original transmission and reflection streams into generation and exchange streams, ensuring that each reorganized stream internally contains complementary information from both source layers. Based on this reorganization, we perform intra-stream self-attention and cross-stream cross-attention computations, with the generation stream serving as the dominant flow. Additionally, we introduce a gating mechanism to precisely regulate the feature fusion process, thereby enhancing the model’s ability to capture inter-layer relationships.

In summary, our main contributions are:

- A novel inter-layer complementary decomposition model decomposing mixed layers into transmission and low-frequency residual layers for dual-stream interaction, with a high-frequency residual layer for reverse fine-tuning, enhancing separation capability while maintaining simplicity.
- A novel inter-layer complementary attention mechanism transforming dual streams into inter-layer complementary structures at the channel dimension for attention computation, significantly improving inter-layer separation.
- Experimental results on multiple standard datasets consistently demonstrate state-of-the-art performance.

## 2 Related Work

### 2.1 Evolution of Physical Modeling Based on inter-Layer Complementarity

Early research [4, 17, 14, 31, 26] often adopted an idealized linear superposition model  $I = T + R$ . Subsequently, to more precisely characterize the asymmetric contributions from the two layers, Wan

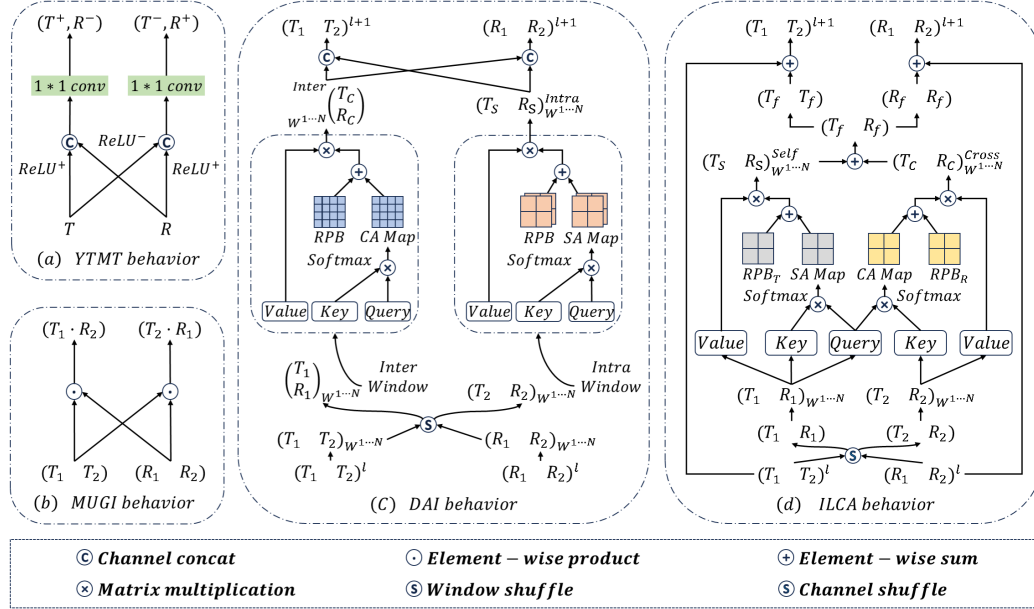


Figure 1: Schematic illustration of dual-stream complementary mechanisms: YTMT, MuGI, DAI, and our proposed inter-layer complementary attention (ILCA). In the notation,  $T_S/R_S$  represent transmission/reflection streams after self-attention,  $T_C/R_C$  after cross-attention, and  $T_f/R_f$  are the final output variables for each stream.

et al. [23] proposed the  $I = \alpha T + \beta R$  model. Variants, such as  $I = \alpha T + R$  used by Li et al. [15] and  $I = \alpha T + (1 - \alpha)R$  employed by Yang et al. [30], introduced mixing coefficients  $\alpha$  and  $\beta$  to quantify the complementary attenuation or enhancement characteristics between layers.

Later research recognized the spatial non-uniformity of reflection phenomena. Dong et al. [2] introduced  $I = W \circ T + R$ , while Wen et al. [27] proposed  $I = W \circ T + (1 - W) \circ R$ . These approaches utilized spatially varying weight maps  $W$  (i.e., Alpha Matting maps, where  $\circ$  denotes element-wise multiplication) that enable the transmission and reflection layers at different pixel locations to be mixed with varying weights, but essentially confined to a linear mixing framework

To overcome the limitations of linear models, Zheng et al. [33] considered the effects of absorption on reflection and refraction, proposing the  $I = \Omega T + \Phi R$ , where  $\Omega$  and  $\Phi$  are spatially varying amplitude coefficient maps. Wan et al. [24] formulated the relationship as  $I = g(T_s) + f(R_s)$ , where  $g(\cdot)$  and  $f(\cdot)$  are nonlinear functions learned by the network that capture their respective degradation processes, with  $T_s$  and  $R_s$  representing the original scenes. Recently, the general framework  $I = \tilde{T} + \tilde{R} + \varphi(T, R)$  proposed by Hu and Guo [10] marked a significant advancement toward nonlinear complementary modeling by introducing a learnable nonlinear residual function  $\varphi(T, R)$  to characterize complex inter-layer interactions and their respective degradation processes.

Beyond direct improvements to physical mixing models, Zhu et al. [35] discovered that hue maps can effectively describe reflection characteristics. Li et al. [15] utilized residual maps to help networks separate components that differ from the main transmission layer. Furthermore, Lei et al. [13] demonstrated that polarization information, due to its strong correlation with reflected light, can provide a physical basis for distinguishing between transmitted and reflected light. Recently, research by Zhong et al. [34] has extended the concept of auxiliary information to the multimodal domain, using natural language descriptions to guide layer separation.

## 2.2 Complementarity Modeling Based on Deep Learning

Although multiple-image solutions have shown satisfactory performance facing weaker ill-posedness [19, 1, 6, 7, 8, 21, 16, 20, 28, 29], their dependence on specific capture mechanisms, such as rotating polarizers or moving cameras, limits their broad applicability. This limitation has motivated a strong focus on single-image reflection removal (SIRR) techniques. Within this area of SIRR, some early

multi-stage methods or those with specific module designs leveraged layer complementarity indirectly. For example, RAGNet [18] first estimates the reflection layer and then utilizes this information to recover the transmission layer through feature differencing and mask guidance. Similarly, CoRRN [25] constructed a collaborative framework that achieves image restoration through a shared encoder and multi-scale gradient guidance. DMGN [5], in its coarse-to-fine generation process, employs preliminarily separated noise as explicit contrastive cues and spatial masks to guide background refinement.

In subsequent research, Hu and Guo et al. conducted a series of explorations in explicitly modeling inter-layer complementarity. In their early YTMT strategy [9], features suppressed in one stream were passed to the counterpart via ReLU and its negative counterpart  $\text{ReLU}^-$ , thereby achieving direct complementarity at the feature level. In their subsequent work, DSRNet [10], this interaction mechanism evolved into the "Mutual Gated Interaction (MuGI)" mechanism, which dynamically controls the exchange of features between the two streams by learning gating signals. Recently, in DSIT [11], they further upgraded the interaction mechanism to "Dual Attention Interaction structure (DAI)." This structure includes both Dual-Stream Self-Attention to capture intra-layer correlations and Layer-aware Dual-Stream Cross-Attention to explicitly model inter-layer correlations.

Research exploring complementarity from different perspectives has also made significant progress. RDNet [32], from an information preservation perspective, designed a Multi-column Reversible Encoder (MCRE), ensuring lossless information transfer and effective utilization during interaction via reversible transformations. DExNet [12], on the other hand, constructs its network by deep unfolding an iterative Sparse and Auxiliary Feature Update (i-SAFU) algorithm which iteratively identifies and penalizes commonalities between transmission and reflection features.

### 3 Methodology

Our overall architecture is illustrated in Fig. 2. First, we propose a novel inter-layer complementary decomposition model (ILCDM) that decomposes the mixed layer into a transmission layer and low-frequency residual layer for dual-stream interaction, and a high-frequency residual layer for reverse adjustment of the dual-stream results. Second, we propose a novel inter-layer complementary attention block (ILCAB) that enhances the inter-layer separation performance of feature flows by utilizing the inter-layer complementary structure. Finally, utilizing the above improvements, we transform Dual-Stream Interactive Transformers (DSIT) into Inter-Layer Complementary Transformer (ILCT).

#### 3.1 Inter-layer Complementary Decomposition Model

We propose an ILCDT for precise demixing of blended images. This model innovatively decomposes the mixed image into three key components:

$$I = T + R_{low} + R_{high} \quad (1)$$

where  $I$  represents the mixed layer,  $T$  denotes the transmission layer,  $R_{low}$  represents the low-frequency residual layer, and  $R_{high}$  denotes the high-frequency residual layer. The specific demixing process is as follows:

$$(\hat{T}, \hat{R}_{low}) = \mathcal{F}_{dual}(I), \quad \hat{R}_{high} = \mathcal{G}(\hat{T}, \hat{R}_{low}) \quad (2)$$

where  $\mathcal{F}_{dual}$  represents the dual-architecture Inter-layer complementary encoder-decoder, whose function is to decompose the mixed layer  $I$  into transmission layer estimate  $\hat{T}$  and low-frequency residual layer estimate  $\hat{R}_{low}$ ;  $\mathcal{G}$  denotes the high-frequency Inter-layer complementary Block, which integrates information from transmission layer estimate  $\hat{T}$  and low-frequency residual layer estimate  $\hat{R}_{low}$  to generate high-frequency residual layer estimate  $\hat{R}_{high}$ , whose role is to finely tune the reconstruction details of the transmission layer.

**Inter-layer Complementary Loss.** Considering the distinct characteristics of low and high frequency components in residual layers, we decompose the residual layer into  $R_{low}$  and  $R_{high}$ . The

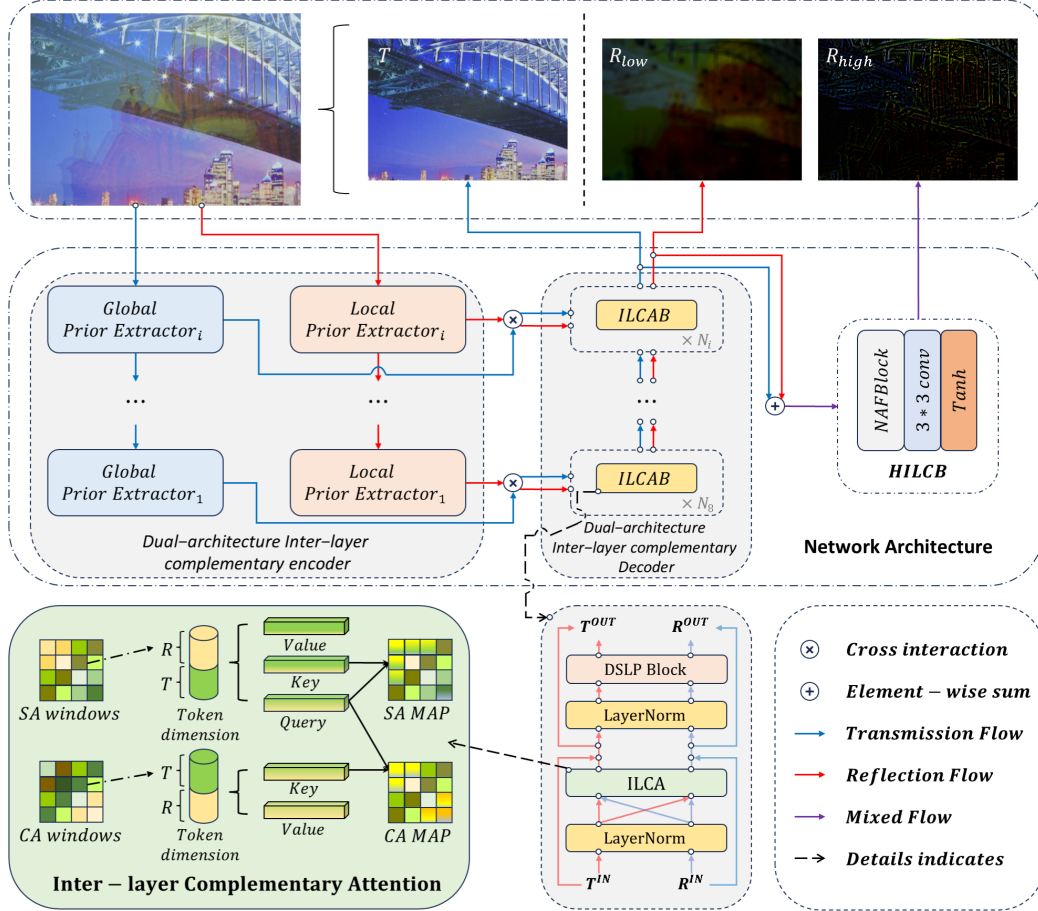


Figure 2: At the top is our proposed Physical Model. The central part details the model’s architecture, which include dual-architecture Inter-layer complementary encoder-decoder, and a high-frequency Inter-layer complementary Block (HILCB). The bottom section shows the location and a visual illustration of our proposed inter-layer complementary attention (ILCA).

low-frequency complementary loss  $L_{\text{freq-low}}$  guides the network to learn low-frequency residual components through two constraints: spatial consistency between the predicted and actual low-frequency residual, and gradient domain consistency to capture robust dual degradation cues from both transmission and reflection. The high-frequency residual loss  $L_{\text{freq-high}}$  focuses on learning high-frequency details obtained by subtracting low-frequency components from the total residual, enabling effective separation of edges, textures, and other fine-grained features. The loss functions are defined as follows:

$$\begin{cases} L_{\text{freq-low}} = \|\hat{R}_{\text{low}} - \|\mathcal{M}(I) - \mathcal{M}(\hat{T})\|_1\|_2^2 + \|\nabla \hat{R}_{\text{low}} - \nabla \|\mathcal{M}(I) - \mathcal{M}(\hat{T})\|_1\|_2^2, \\ L_{\text{freq-high}} = \|\hat{R}_{\text{high}} - \|I - \hat{T} - (\mathcal{M}(I) - \mathcal{M}(\hat{T}))\|_1\|_1, \end{cases} \quad (3)$$

where  $\mathcal{M}(\cdot)$  denotes the mean filtering operation for extracting low-frequency information from images.  $\nabla$  represents the gradient operator, used to compute image gradients in horizontal and vertical directions.  $\|\cdot\|_1$  and  $\|\cdot\|_2$  denote the  $\ell_1$  and  $\ell_2$  norms, respectively.

### 3.2 Inter-layer Complementary Attention Block

As shown in Fig. 2, we present an ILCAB in the dual-architecture Inter-layer complementary encoder-decoder. This module first simultaneously receives the transmission flow ( $F_T^{IN}$ ) and complementary flow ( $F_C^{IN}$ ) as inputs. Subsequently, layer normalization is applied to both input flows, followed by Inter-layer complementary attention mechanism (ILCAM) processing. Finally, the processing results

are enhanced through layer normalization and feed-forward network in the ILCAB, yielding feature flows  $F_T^{OUT}$  and  $F_C^{OUT}$ . We provide detailed explanations about the ILCAM in the remaining part of this subsection.

**Inter-layer Complementary Attention Mechanism.** As shown in Fig. 1, We propose a novel ILCAM applied to the dual-architecture Inter-layer complementary encoder-decoder. Specifically, when we obtain the transmission feature flow  $F_T \in \mathbb{R}^{N \times C}$  and residual feature flow  $F_R \in \mathbb{R}^{N \times C}$ , we first need to split each flow into two parts along the channel dimension:

$$F_T = [F_{T1}, F_{T2}], \quad F_R = [F_{R1}, F_{R2}] \quad (4)$$

In this expression,  $F_{T1}, F_{T2}, F_{R1}, F_{R2} \in \mathbb{R}^{N \times \frac{C}{2}}$  represent the split features, with each part containing half of the original channel dimension. Subsequently, we cross-combine these channel-split features to form two new feature flows: generation flow and exchange flow:

$$F_{Gen} = [F_{T1}, F_{R1}], \quad F_{Exch} = [F_{T2}, F_{R2}] \quad (5)$$

where the generation flow  $F_{Gen}$  fuses the first half of transmission and complementary feature channels, while the exchange flow  $F_{Exch}$  contains the remaining second half of channels. Next, we perform intra-flow self-attention computation on the generation flow and cross-flow cross-attention computation from the generation flow to the exchange flow, generating corresponding query, key, and value matrices through the following linear transformations:

$$\begin{cases} Q_{Gen} = F_{Gen}W_{q1}, & K_{Gen} = F_{Gen}W_{k1}, & V_{Gen} = F_{Gen}W_{v1} \\ Q_{Cross} = F_{Gen}W_{q2}, & K_{Cross} = F_{Exch}W_{k2}, & V_{Cross} = F_{Exch}W_{v2}, \end{cases} \quad (6)$$

These matrices are obtained by applying weight matrices  $W_{q1}, W_{k1}, W_{v1} \in \mathbb{R}^{C \times D}$  and  $W_{q2}, W_{k2}, W_{v2} \in \mathbb{R}^{C \times D}$  through linear transformations, projecting the original  $C$ -dimensional features to the  $D$ -dimensional hidden representation space.

In intra-flow self-attention, queries, keys, and values all originate from the generation flow, while in cross-flow attention, queries come from the generation flow, and keys and values come from the exchange flow. This design effectively promotes deep information interaction between the two feature flows. For computational efficiency, we adopt window-based attention mechanism to reduce computational complexity from  $O(N^2)$  to  $O(N_W \cdot N)$ . Under this mechanism,  $Q_{Gen}, K_{Gen}, V_{Gen} \in \mathbb{R}^{2N_T \times N_W \times D}$  and  $Q_{Cross}, K_{Cross}, V_{Cross} \in \mathbb{R}^{2N_T \times N_W \times D}$ , where  $N_T$  represents the total number of windows, and  $N_W$  represents the window size. Based on the above components, the complete intra-flow self-attention and cross-flow attention operations can be expressed as:

$$\begin{cases} Y_{Intra} = \text{Intra-SA}(Q_{Gen}, K_{Gen}, V_{Gen}) = \text{SoftMax}(Q_{Gen}K_{Gen}^\top / \sqrt{D} + B_{Intra})V_{Gen} \\ Y_{Cross} = \text{Cross-A}(Q_{Cross}, K_{Cross}, V_{Cross}) = \text{SoftMax}(Q_{Cross}K_{Cross}^\top / \sqrt{D} + B_{Cross})V_{Cross}, \end{cases} \quad (7)$$

To enhance the model's spatial awareness capability, we introduce a relative position bias mechanism. Intra-flow self-attention bias  $B_{Intra} \in \mathbb{R}^{N_W \times N_W}$  and cross-flow cross-attention bias  $B_{Cross} \in \mathbb{R}^{N_W \times N_W}$  are obtained by indexing learnable lookup tables  $B_{Intra}^{LUT} \in \mathbb{R}^{(2\sqrt{N_W}-1) \times (2\sqrt{N_W}-1)}$  and  $B_{Cross}^{LUT} \in \mathbb{R}^{(2\sqrt{N_W}-1) \times (2\sqrt{N_W}-1)}$ , respectively. These lookup tables contain all possible relative position combinations. We fuse the results of both attention operations:

$$F_{Combined} = Y_{Intra} + Y_{Cross} \quad (8)$$

Finally, to ensure  $F_T^{final}$  and  $F_R^{final}$  maintain the same channel dimension  $C$  as the original inputs  $F_T$  and  $F_R$ , we first split  $F_{Combined}$  along the channel dimension to recover transmission and complementary features, then ensure dimensional consistency through duplication operations:

$$[F'_T, F'_R] = F_{Combined}, \quad F_T^{final} = [F'_T, F'_T], \quad F_R^{final} = [F'_R, F'_R] \quad (9)$$

Table 1: Quantitative results on five real-world testing datasets of SIRS models and their averages. The best results are displayed in **bold**, and the second-best are underlined.  $\triangle$  means that official pretrained weights are used.

| Methods                    | Real20 (20)  |              | Objects (200) |              | Postcard (199) |              | Wild (55)    |              | Nature(20)   |              | Average (494) |              |
|----------------------------|--------------|--------------|---------------|--------------|----------------|--------------|--------------|--------------|--------------|--------------|---------------|--------------|
|                            | PSNR         | SSIM         | PSNR          | SSIM         | PSNR           | SSIM         | PSNR         | SSIM         | PSNR         | SSIM         | PSNR          | SSIM         |
| Li et al $\triangle$ [15]  | 21.85        | 0.777        | 24.95         | 0.899        | 23.45          | 0.879        | 24.35        | 0.886        | 24.03        | 0.798        | 24.11         | 0.881        |
| Dong et al $\triangle$ [2] | 23.08        | 0.826        | 24.16         | 0.899        | 24.27          | 0.907        | 26.03        | 0.900        | 23.66        | 0.819        | 24.35         | 0.896        |
| DSRNet $\triangle$ [10]    | 23.85        | 0.809        | 26.88         | 0.923        | 24.72          | 0.915        | 27.04        | 0.915        | 25.27        | 0.836        | 25.84         | 0.910        |
| HGRR $\triangle$ [35]      | 23.78        | 0.818        | 25.11         | 0.902        | 23.85          | 0.900        | 27.05        | 0.900        | 25.51        | 0.827        | 24.78         | 0.895        |
| RRW $\triangle$ [13]       | 21.93        | 0.788        | 26.89         | 0.925        | 24.29          | 0.887        | 26.82        | 0.910        | 26.14        | 0.846        | 25.60         | 0.899        |
| DSIT $\triangle$ [11]      | 25.19        | <u>0.834</u> | 26.87         | 0.925        | <u>26.38</u>   | <u>0.925</u> | <u>27.90</u> | <b>0.923</b> | <u>26.68</u> | <u>0.847</u> | 26.71         | <u>0.918</u> |
| RDNNet $\triangle$ [32]    | <b>25.71</b> | <b>0.850</b> | <u>26.95</u>  | <u>0.926</u> | 26.33          | 0.922        | 27.84        | 0.917        | 26.31        | 0.846        | <u>26.72</u>  | 0.917        |
| Ours                       | <u>25.12</u> | 0.828        | <b>27.07</b>  | <b>0.930</b> | <b>26.43</b>   | <b>0.931</b> | <b>27.96</b> | <u>0.922</u> | <b>27.03</b> | <b>0.853</b> | <b>26.83</b>  | <b>0.922</b> |

$$[F'_T, F'_R] = F_{Combined}, \quad F_T^{final} = [F'_T, F'_T], \quad F_R^{final} = [F'_R, F'_R] \quad (10)$$

### 3.3 Loss Function

**Pixel reconstruction loss.** To achieve consistency of  $\hat{\mathbf{T}}$ ,  $\hat{\mathbf{R}}_{low}$ , and  $\hat{\mathbf{R}}_{high}$  with their corresponding supervision labels in the spatial domain, we introduce the following loss function:

$$\begin{aligned} \mathcal{L}_{pix} := & \|\hat{\mathbf{T}} - \mathbf{T}\|_2^2 + \|\hat{\mathbf{R}}_{low} - \|\mathcal{M}(I) - \mathcal{M}(\hat{T})\|_1\|_2^2 + \\ & \alpha \|\hat{\mathbf{R}}_{high} - \|I - \hat{T} - (\mathcal{M}(I) - \mathcal{M}(\hat{T}))\|_1\|_1 \end{aligned} \quad (11)$$

where  $\|\cdot\|_2$  and  $\|\cdot\|_1$  denote the  $\ell_2$  and  $\ell_1$  norms, respectively.  $\mathcal{M}(\cdot)$  extracts low-frequency information from images through mean filtering.  $\alpha$  is a hyperparameter used to balance the fidelity of the high-frequency residual layer estimation and other layer estimation.

**Gradient Reconstruction Loss.** Considering gradient independence, as a traditional prior in blind source separation, we simultaneously encourage the model to recover true gradients and penalize intersecting gradients as follows:

$$\begin{aligned} \mathcal{L}_{grad} := & \|\nabla\hat{\mathbf{T}} - \nabla\mathbf{T}\|_1 + \|\nabla\hat{\mathbf{R}}_{low} - \nabla\|\mathcal{M}(I) - \mathcal{M}(\hat{T})\|_1\|_2^2 + \frac{1}{N} \sum_{n=0}^{N-1} \beta \|\mathcal{D}(\hat{\mathbf{T}}^{\downarrow n}, \hat{\mathbf{R}}_{low}^{\downarrow n})\|_2^2, \\ \mathcal{D}(\hat{\mathbf{T}}, \hat{\mathbf{R}}_{low}) := & \tanh(\xi_1 |\nabla\hat{\mathbf{T}}|) \circ \tanh(\xi_2 |\nabla\hat{\mathbf{R}}_{low}|), \end{aligned} \quad (12)$$

where  $\nabla$  denotes the difference operator of images.  $\hat{\mathbf{T}}^{\downarrow n}$ ,  $\hat{\mathbf{R}}_{low}^{\downarrow n}$  are  $2^n$  downsampled versions of  $\hat{\mathbf{T}}$  and  $\hat{\mathbf{R}}_{low}$ .  $\xi_1$  and  $\xi_2$  are normalization factors. The multi-scale exclusion term  $\mathcal{D}$  achieves gradient exclusivity between the transmission layer and low-frequency residual layer through the tanh function and element-wise multiplication ( $\circ$ ).

**Feature reconstruction loss.** To enhance the perceptual quality of decoupled layers, we utilize the following feature reconstruction loss:

$$\mathcal{L}_{fea} := \sum_i \omega_i \|\phi_i(\hat{\mathbf{T}}) - \phi_i(\mathbf{T})\|_1, \quad (13)$$

where  $\phi_i(\cdot)$  represents the intermediate features of the pretrained VGG-19 model, with  $i \in \{2, 7, 12, 21, 30\}$  indicating layer IDs.  $\omega_i$  balances the weights of different hierarchies.

**Total Loss.** The complete training objective  $\mathcal{L}_{total}$  is defined as follows:

$$\mathcal{L}_{total} := \lambda_1 \mathcal{L}_{pix} + \lambda_2 \mathcal{L}_{grad} + \lambda_3 \mathcal{L}_{fea}, \quad (14)$$

where  $\lambda_1 = 1$ ,  $\lambda_2 = 1$ , and  $\lambda_3 = 0.01$  are coefficients for balancing different loss terms.

## 4 Experimental Validation

### 4.1 Implementation Details

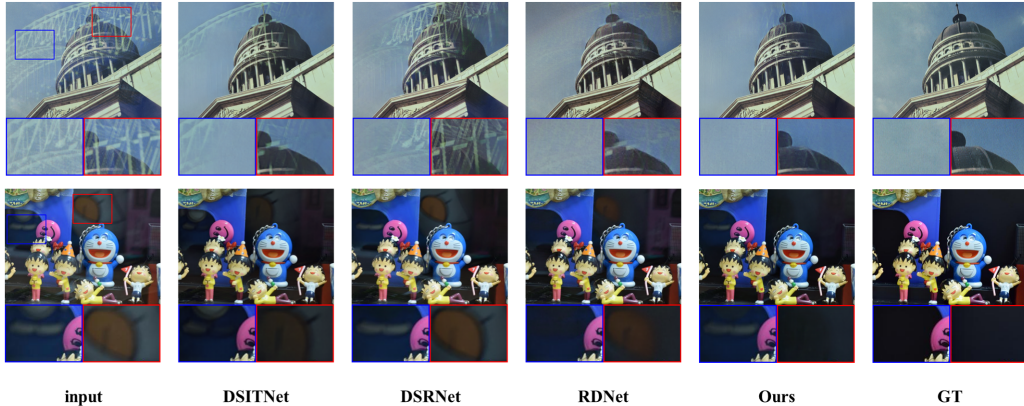


Figure 3: Visual comparison of transmission layer predictions between previous state-of-the-art methods and ours on samples from the Postcard and SolidObject datasets. The boxed regions highlight magnified views of local areas for detailed inspection.

We constructed a comprehensive training dataset comprising 500 synthetic image pairs from the PASCAL VOC dataset [3], 90 real image pairs from [31], and 200 image pairs from the “Nature” dataset [15]. All images were preprocessed and resized to  $384 \times 384$  pixels. Our training strategy used 4000 image pairs per epoch with a  $0.6 : 0.2 : 0.2$  distribution ratio for synthetic, real, and Nature data, respectively. The model was implemented in PyTorch and trained for 120 epochs using the Adam optimizer with a learning rate of  $10^{-4}$  and batch size of 1. For attention mechanisms, we set the window size  $N_W$  to  $12 \times 12$ , while  $N_T$  was dynamically adjusted based on feature spatial scales. All experiments were conducted on a single NVIDIA RTX 4090 GPU.

## 4.2 Performance Evaluation

**Quantitative comparison.** As shown in Tab. 1, our proposed method achieves excellent average performance metrics on five real-world benchmark datasets, with particularly outstanding performance on the  $SIR^2$  [22] dataset containing complex reflection scenarios. This superior performance stems from our two key innovations based on inter-layer complementarity: first, an inter-layer complementary decomposition model that better captures the image unmixing mechanism, and second, an inter-layer complementary attention mechanism that more effectively performs feature flow separation between layers. The effectiveness of our

approach extends beyond performance gains to computational efficiency. As shown in Tab. 2, our proposed LCAB significantly outperforms the baseline DAIB, reducing computational operations

Table 2: Performance comparison between attention mechanisms.

| Factors         | Instances | Indicators    |               |               |
|-----------------|-----------|---------------|---------------|---------------|
|                 |           | Params(M)     | FLOPs(G)      | Speed(ms)     |
| Attention Block | DAIB      | 326.96        | 433.85        | 224.24        |
|                 | LCAB      | <b>326.74</b> | <b>338.49</b> | <b>194.28</b> |

Table 3: Ablation study on different factors of our design. † means our data settling is employed to train the model. \* means gradient loss using MSE loss

| Factors            | Instances         | Real20 (20)  |              | Nature (20)  |              | SIR <sup>2</sup> (454) |              |
|--------------------|-------------------|--------------|--------------|--------------|--------------|------------------------|--------------|
|                    |                   | PSNR         | SSIM         | PSNR         | SSIM         | PSNR                   | SSIM         |
| Physical Model     | YTMT-R†           | 22.21        | 0.794        | 23.89        | 0.820        | 24.03                  | 0.894        |
|                    | YTMT-C†           | 22.75        | 0.804        | 24.10        | 0.818        | 24.15                  | 0.894        |
|                    | DSR-R†            | 23.31        | 0.802        | 24.43        | 0.829        | 25.98                  | 0.918        |
|                    | DSR-C†            | 23.72        | 0.824        | 24.74        | 0.843        | 26.09                  | 0.916        |
|                    | DSIT-R†           | 24.85        | <b>0.824</b> | 26.28        | 0.847        | 26.40                  | 0.924        |
|                    | DSIT-C†           | 24.90        | <b>0.830</b> | 26.50        | <b>0.850</b> | <b>26.72</b>           | <b>0.929</b> |
| Filter Kernel Size | DSIT-C†*          | <b>25.08</b> | 0.829        | <b>26.95</b> | 0.846        | 26.55                  | 0.925        |
|                    | None†*            | 25.04        | 0.830        | 26.77        | 0.852        | 26.69                  | 0.924        |
|                    | $1 \times 1$ †*   | 25.08        | 0.829        | 26.98        | 0.853        | 26.70                  | 0.926        |
|                    | $7 \times 7$ †*   | 25.10        | 0.831        | 26.60        | 0.851        | 26.82                  | 0.928        |
|                    | $13 \times 13$ †* | <b>25.12</b> | 0.828        | <b>27.03</b> | <b>0.853</b> | <b>26.90</b>           | <b>0.929</b> |
| Attention Block    | $25 \times 25$ †* | 24.82        | <b>0.831</b> | 26.90        | 0.852        | 26.67                  | 0.925        |
|                    | DAIB†*            | 24.58        | 0.827        | 25.94        | 0.845        | 26.72                  | 0.928        |
|                    | CSAB†*            | <b>25.40</b> | <b>0.830</b> | 26.52        | 0.847        | 26.38                  | 0.926        |
|                    | LCAB†*            | 25.12        | 0.828        | <b>27.03</b> | <b>0.853</b> | <b>26.90</b>           | <b>0.929</b> |

by approximately 22% and improving processing speed by about 13.4% while maintaining nearly identical parameter count. This further validates the importance and practicality of designing modules based on inter-layer complementarity principles.

#### Qualitative comparison.

We conduct a comparative analysis using two representative cases: strong reflection scenes from the Postcard dataset and weak reflection scenes from the SolidObject dataset. As demonstrated in Fig. 3, both DSIT and DSRNet methods fail to completely eliminate reflection residuals in strong reflection scenarios, while RDNet, although reducing reflection interference to some extent, introduces color distortion artifacts. These existing approaches continue to exhibit similar issues in weak reflection scenarios, displaying various degrees of reflection residual problems. In contrast, our proposed method demonstrates superior performance across both scenarios by successfully removing reflection layers while accurately preserving the fine details and original colors of the transmission layer, which is primarily attributed to our effective exploitation of inter-layer complementarity.

### 4.3 Ablation Study

**Physical Model.** As shown in Tab. 3, dual-stream architecture methods including YTMT, DSRNet, and DSIT can conveniently integrate our proposed inter-layer complementary loss function to transform into inter-layer complementary decomposition models, achieving significant performance improvements. This enhancement is attributed to the low-frequency residual flow providing more robust reflection and transmission degradation cues for the model’s reflection removal process.

**Filter Kernel Size.** To determine the optimal kernel size for average filtering in the inter-layer complementary loss function, we conducted systematic evaluation experiments with five filter kernel configurations: None,  $1 \times 1$ ,  $7 \times 7$ ,  $13 \times 13$ , and  $25 \times 25$ . Specifically, “None” indicates that the inter-layer complementary demixing model was not used,  $1 \times 1$  means no low-frequency component extraction was applied to the residual layer, while the other three sizes represent progressively increasing degrees of filtering.

The experimental results in Tab. 3 demonstrate that the  $13 \times 13$  filter kernel achieved optimal performance. This kernel size can capture sufficient contextual information while effectively preserving key structural features, avoiding structural loss caused by excessive smoothing, thus achieving performance optimization.

**LCAB Module Design.** To demonstrate the effectiveness of our designed LCAB, we conducted ablation experiments. Specifically, we established two baselines for comparison: the first baseline employs the DAIB module, while the second baseline adopts direct channel-wise concatenation when reorganizing flow structures, rather than our proposed cross-reorganization strategy. As shown in Tab. 3, our LCAB achieves the best performance across all metrics, which can be attributed to its thorough exploitation of inter-layer complementarity.

## 5 Concluding Remarks

This study proposes an inter-layer complementary decomposition model and attention mechanism based on inter-layer complementarity principles. In the decomposition model, we decompose mixed image layers into transmission and low-frequency residual layers for dual-stream interaction, while constructing high-frequency residual layers that utilize dual-stream features to reversely adjust dual-stream results, achieving precise modeling of the image demixing process. In the attention mechanism, we temporarily reorganize dual-stream features into a unified representation with inter-layer complementary structure, enabling attention computation to effectively achieve inter-layer separation of feature streams, then restore the original dual-stream structure after computation. Experimental results show our method outperforms existing state-of-the-art techniques across multiple real-world benchmark datasets, fully demonstrating robustness and adaptability in complex reflection scenarios. Additionally, comprehensive ablation studies validate the effectiveness of each key component, confirming the superiority of our design choices. Overall, this work expands new perspectives for reflection removal research and brings inspiration to other image decomposition tasks.

## 6 Limitations

Current single image reflection removal methods often struggle to completely eliminate reflections in challenging scenarios, frequently introducing color degradation and artifacts. Although our proposed method achieves significant improvements in addressing these issues, there remains considerable room for further enhancement. To this end, the performance of our method can be further improved by collecting richer real-world datasets.

## References

- [1] Amit Agrawal, Ramesh Raskar, Shree K Nayar, and Yuanzhen Li. Removing photography artifacts using gradient projection and flash-exposure sampling. In *ACM SIGGRAPH 2005 Papers*, pages 828–835. 2005.
- [2] Zheng Dong, Ke Xu, Yin Yang, Hujun Bao, Weiwei Xu, and Rynson WH Lau. Location-aware single image reflection removal. In *Proceedings of the IEEE/CVF international conference on computer vision*, pages 5017–5026, 2021.
- [3] Mark Everingham, Luc Van Gool, Christopher KI Williams, John Winn, and Andrew Zisserman. The pascal visual object classes (voc) challenge. *International journal of computer vision*, 88:303–338, 2010.
- [4] Qingnan Fan, Jiaolong Yang, Gang Hua, Baoquan Chen, and David Wipf. A generic deep architecture for single image reflection removal and image smoothing. In *Proceedings of the IEEE International Conference on Computer Vision*, pages 3238–3247, 2017.
- [5] Xin Feng, Wenjie Pei, Zihui Jia, Fanglin Chen, David Zhang, and Guangming Lu. Deep-masking generative network: A unified framework for background restoration from superimposed images. *IEEE Transactions on Image Processing*, 30:4867–4882, 2021.
- [6] Kun Gai, Zhenwei Shi, and Changshui Zhang. Blind separation of superimposed moving images using image statistics. *IEEE transactions on pattern analysis and machine intelligence*, 34(1):19–32, 2011.
- [7] Xiaojie Guo, Xiaochun Cao, and Yi Ma. Robust separation of reflection from multiple images. In *Proceedings of the IEEE conference on computer vision and pattern recognition*, pages 2187–2194, 2014.
- [8] Byeong-Ju Han and Jae-Young Sim. Reflection removal using low-rank matrix completion. In *Proceedings of the IEEE Conference on Computer Vision and Pattern Recognition*, pages 5438–5446, 2017.
- [9] Qiming Hu and Xiaojie Guo. Trash or treasure? an interactive dual-stream strategy for single image reflection separation. *Advances in Neural Information Processing Systems*, 34:24683–24694, 2021.
- [10] Qiming Hu and Xiaojie Guo. Single image reflection separation via component synergy. In *Proceedings of the IEEE/CVF International Conference on Computer Vision*, pages 13138–13147, 2023.
- [11] Qiming Hu, Hainuo Wang, and Xiaojie Guo. Single image reflection separation via dual-stream interactive transformers. *Advances in Neural Information Processing Systems*, 37:55228–55248, 2024.
- [12] Jun-Jie Huang, Tianrui Liu, Zihan Chen, Xinwang Liu, Meng Wang, and Pier Luigi Dragotti. A lightweight deep exclusion unfolding network for single image reflection removal. *IEEE Transactions on Pattern Analysis and Machine Intelligence*, 2025.
- [13] Chenyang Lei, Xuhua Huang, Mengdi Zhang, Qiong Yan, Wenxiu Sun, and Qifeng Chen. Polarized reflection removal with perfect alignment in the wild. In *Proceedings of the IEEE/CVF conference on computer vision and pattern recognition*, pages 1750–1758, 2020.

- [14] Anat Levin and Yair Weiss. User assisted separation of reflections from a single image using a sparsity prior. *IEEE Transactions on Pattern Analysis and Machine Intelligence*, 29(9):1647–1654, 2007.
- [15] Chao Li, Yixiao Yang, Kun He, Stephen Lin, and John E Hopcroft. Single image reflection removal through cascaded refinement. In *Proceedings of the IEEE/CVF conference on computer vision and pattern recognition*, pages 3565–3574, 2020.
- [16] Yu Li and Michael S Brown. Exploiting reflection change for automatic reflection removal. In *Proceedings of the IEEE international conference on computer vision*, pages 2432–2439, 2013.
- [17] Yu Li and Michael S Brown. Single image layer separation using relative smoothness. In *Proceedings of the IEEE conference on computer vision and pattern recognition*, pages 2752–2759, 2014.
- [18] Yu Li, Ming Liu, Yaling Yi, Qince Li, Dongwei Ren, and Wangmeng Zuo. Two-stage single image reflection removal with reflection-aware guidance. *Applied Intelligence*, 53(16):19433–19448, 2023.
- [19] Bernard Sarel and Michal Irani. Separating transparent layers through layer information exchange. In *Computer Vision-ECCV 2004: 8th European Conference on Computer Vision, Prague, Czech Republic, May 11-14, 2004. Proceedings, Part IV 8*, pages 328–341. Springer, 2004.
- [20] Christian Simon and In Kyu Park. Reflection removal for in-vehicle black box videos. In *Proceedings of the IEEE Conference on Computer Vision and Pattern Recognition*, pages 4231–4239, 2015.
- [21] Sudipta N Sinha, Johannes Kopf, Michael Goesele, Daniel Scharstein, and Richard Szeliski. Image-based rendering for scenes with reflections. *ACM Transactions on Graphics (TOG)*, 31(4):1–10, 2012.
- [22] Renjie Wan, Boxin Shi, Ling-Yu Duan, Ah-Hwee Tan, and Alex C Kot. Benchmarking single-image reflection removal algorithms. In *Proceedings of the IEEE International Conference on Computer Vision*, pages 3922–3930, 2017.
- [23] Renjie Wan, Boxin Shi, Ling-Yu Duan, Ah-Hwee Tan, and Alex C Kot. Crnn: Multi-scale guided concurrent reflection removal network. In *Proceedings of the IEEE Conference on Computer Vision and Pattern Recognition*, pages 4777–4785, 2018.
- [24] Renjie Wan, Boxin Shi, Haoliang Li, Ling-Yu Duan, and Alex C Kot. Reflection scene separation from a single image. In *Proceedings of the IEEE/CVF Conference on Computer Vision and Pattern Recognition*, pages 2398–2406, 2020.
- [25] Renjie Wan, Boxin Shi, Haoliang Li, Ling-Yu Duan, Ah-Hwee Tan, and Alex C Kot. Corrn: Cooperative reflection removal network. *IEEE transactions on pattern analysis and machine intelligence*, 42(12):2969–2982, 2019.
- [26] Kaixuan Wei, Jiaolong Yang, Ying Fu, David Wipf, and Hua Huang. Single image reflection removal exploiting misaligned training data and network enhancements. In *Proceedings of the IEEE/CVF Conference on Computer Vision and Pattern Recognition*, pages 8178–8187, 2019.
- [27] Qiang Wen, Yinjie Tan, Jing Qin, Wenxi Liu, Guoqiang Han, and Shengfeng He. Single image reflection removal beyond linearity. In *Proceedings of the IEEE/CVF Conference on Computer Vision and Pattern Recognition*, pages 3771–3779, 2019.
- [28] Tianfan Xue, Michael Rubinstein, Ce Liu, and William T Freeman. A computational approach for obstruction-free photography. *ACM Transactions on Graphics (TOG)*, 34(4):1–11, 2015.
- [29] Jiaolong Yang, Hongdong Li, Yuchao Dai, and Robby T Tan. Robust optical flow estimation of double-layer images under transparency or reflection. In *Proceedings of the IEEE Conference on Computer Vision and Pattern Recognition*, pages 1410–1419, 2016.

- [30] Jie Yang, Dong Gong, Lingqiao Liu, and Qinfeng Shi. Seeing deeply and bidirectionally: A deep learning approach for single image reflection removal. In *Proceedings of the european conference on computer vision (ECCV)*, pages 654–669, 2018.
- [31] Xuaner Zhang, Ren Ng, and Qifeng Chen. Single image reflection separation with perceptual losses. In *Proceedings of the IEEE conference on computer vision and pattern recognition*, pages 4786–4794, 2018.
- [32] Hao Zhao, Mingjia Li, Qiming Hu, and Xiaojie Guo. Reversible decoupling network for single image reflection removal. *arXiv preprint arXiv:2410.08063*, 2024.
- [33] Qian Zheng, Boxin Shi, Jinnan Chen, Xudong Jiang, Ling-Yu Duan, and Alex C Kot. Single image reflection removal with absorption effect. In *Proceedings of the IEEE/CVF Conference on Computer Vision and Pattern Recognition*, pages 13395–13404, 2021.
- [34] Haofeng Zhong, Yuchen Hong, Shuchen Weng, Jinxiu Liang, and Boxin Shi. Language-guided image reflection separation. In *Proceedings of the IEEE/CVF Conference on Computer Vision and Pattern Recognition*, pages 24913–24922, 2024.
- [35] Yurui Zhu, Xueyang Fu, Zheyu Zhang, Aiping Liu, Zhiwei Xiong, and Zheng-Jun Zha. Hue guidance network for single image reflection removal. *IEEE transactions on neural networks and learning systems*, 2023.